Materials Science & Engineering C 117 (2020) 111345

Contents lists available at ScienceDirect

Materials Science & Engineering C

journal homepage: www.elsevier.com/locate/msec

A CNT-PDMS wearable device for simultaneous measurement of wrist pulse pressure and cardiac electrical activity

Li Wang[a,1], Wenkun Dou[b,1], Jun Chen[a,*], Kechao Lu[a], Feng Zhang[a], Mohammed Abdulaziz[c], Weiguang Su[a], Anqing Li[a], Chonghai Xu[a,*], Yu Sun[b,*]

[a] Advanced Micro and Nanoinstruments Center (AMNC), School of Mechanical & Automotive Engineering, Qilu University of Technology (Shandong Academy of Sciences), Jinan, Shandong 250353, China
[b] Department of Mechanical and Industrial Engineering, University of Toronto, Toronto, ON M5S 3G8, Canada
[c] Department of Mechanical and Process Engineering, University of Duisburg Essen, Forsthausweg 247057, Germany

ARTICLE INFO

Keywords:
Carbon nanotube (CNT)
Polydimethylsiloxane (PDMS)
Wrist pulse pressure
Electrocardiograph (ECG)
Wearable device

ABSTRACT

Simultaneous measurement of multi-physiological signals can provide effective diagnosis and therapeutic assessment of diseases. This paper reports a carbon nanotube (CNT) - Polydimethylsiloxane (PDMS) - based wearable device with piezo-resistive and voltage-sensing capabilities for simultaneously capturing wrist pulse pressure and cardiac electrical signal. The layout design of sensing elements in the device was guided by analyzing strain distribution and electric field distribution for minimizing the interference between wrist pulse and cardiac electric activity during measurement. Each device was preconditioned under the strain of 20% until the resistance change of the device reached equilibrium. After preconditioning, the relationship between the resistance change and the pressure was calibrated, which determined the device sensitivity to be 0.01 Pa^{-1} and the linear pressure range of the device to be 0.4 kPa to 14.0 kPa. Mechanisms of CNT-PDMS for sensing strain signal and electrical pulse signal were explored by scanning electron microscopy (SEM) imaging and equivalent circuit modeling. The device was applied to monitor the wrist pulse and ECG signals of volunteers during the recovering process after physical exercises.

1. Introduction

Health data compiled from more than 190 countries show that heart disease remains a major cause of death globally. Each year, heart diseases lead to approximately 17.3 million deaths in the world [1,2]. Heart undertakes a complex set of actions, including the initiation and propagation of a regular electrical signal (proper heart rate and rhythm) and generating sufficient contraction force, which drives the blood circulation [3,4]. At the cellular level, each cardiomyocyte acts synergistically to achieve a proper beating rate, beating rhythm, and contractile force. Dysfunction in these actions can lead to heart arrhythmia, possibly leading to heart attack, myocardial infarction and other complications [5].

At the organ level, the working status of the heart can be characterized by both the bioelectric and mechanical aspects simultaneously. The action potential generated by the heart sinoatrial node travels through the internodal pathways in the right atrium (RA) to the atrioventricular (AV) node, causing the heart muscle to contract or relax and enabling the heart to pump blood. The increase in blood pressure pushes against the elastic walls of the arteries. The cardiac electrical signal can be recorded by the electrocardiograph (ECG) machine and used for clinical diagnosis of heart diseases [6,7]. For example, an irregular ECG signal is often related to arrhythmia [8,9]. Over 90% of patients with heart failure show an abnormal ECG signal pattern [10]. In the meanwhile, from the mechanical perspective, each heartbeat produces a pulse in the arteries, which can be conveniently measured at the radial wrist artery (e.g., wrist pulse wave) [11,12]. Wrist pulse is an effective mechanical indicator for evaluating cardiac contractility. An irregular wrist pulse can reflect sinus arrhythmia, atrial fibrillation, paroxysmal atrial tachycardia, atrial flutter, partial heart block and heart failure [13–15]. However, the correlation relationship between ECG and wrist pulse wave still remains unknown, especially in the sudden-happened disease status, like a heart attack. The reason is possibly due to the lack of a technique capable of uninterrupted simultaneous measurement of ECG and wrist pulse waves in the long term. Simultaneous measurement of ECG and wrist pulse

* Corresponding authors.
E-mail addresses: chenjun@qlu.edu.cn (J. Chen), xch@qlu.edu.cn (C. Xu), sun@mie.utoronto.ca (Y. Sun).
[1] Authors equally contributed to the work.

https://doi.org/10.1016/j.msec.2020.111345
Received 15 September 2019; Received in revised form 16 June 2020; Accepted 17 July 2020
Available online 11 August 2020
0928-4931/

waves can obtain multi-physiological signals including both bioelectric and mechanical aspects. Uninterrupted monitoring of these signals could effectively capture the sudden events (like heart attack) and generate an early alarm. Besides, it has the potential of providing multi-physiological cardiac signals for clinical diagnosis.

Accordingly, a wearable device is demanded for simultaneous monitoring of ECG and wrist pulse in an uninterrupted potable way, which would avoid the complexity and inconvenience of traditional heart monitoring instruments [16] and hold promise for personalized healthcare [17,18]. Much effort has been spent to develop wearable health monitoring devices by using flexible sensors and electronics during recent years. Miniaturized wrist pulse sensors, such as piezoresistive sensor, capacitive sensor, piezoelectric sensor, and triboelectric sensor, are used in wearable devices [19,20]. Many kinds of stretchable and conductive nanocomposites have been widely applied in biosignal measurement due to its high specific surface area and elastomeric property, including gold nanoparticles-epoxy, graphene-PDMS, CNT-PDMS [2,8–11]. Among these materials, the one-dimensional nanomaterials including CNT and metallic nanowires are the ideal filler materials because they have more inter-connections to lower the percolation threshold, leading to high conductivity [8]. Compared to precious metallic nanowires, the cost of using CNT could be significantly reduced in the flexible device, which makes CNT widely adopted in health monitoring devices. For example, carbon nanotube (CNT)-PDMS material was fabricated into a stretchable strain sensor for measuring blood pressure and wrist pulse [21–24]. Flexible electrodes have been developed to replace the traditional rigid Ag/AgCl electrode for ECG monitoring in wearable devices [6,25]. However, these existing wearable devices cannot simultaneously measure ECG and wrist pulse wave due to the interference between the mechanical deformation of the skin and the electrical field of ECG in the sensor. For example, ECG signals measured at the chest are often disturbed by lung respiration due to the changes in the distance and contact area between skin and electrodes [22,26,27]. Meanwhile, ECG signal on the skin surface may affect the readout of the flexible piezoresistive strain sensor that was designed to measure the mechanical wrist pulse pressure because the flexible piezoresistive material contains conductive nanocomposite (e.g., gold nanoparticle, carbon nanotube or graphene flakes) that can also capture the electric signal as false resistive changes [28,29]. The interference of multi-physiological signals remains a key challenge in existing wearable devices [30].

This paper focuses on solving the problem of the interference between the mechanical deformation of the skin and the electrical field of ECG. The device consists of a flexible piezoresistive strain sensor for monitoring the wrist pulse and capacitive electrodes for monitoring cardiac electric activity. The layout of the sensing elements including the strain sensor and capacitive electrodes was optimized via finite element analysis (FEA) to minimize the interference between the mechanical deformation of the skin and the electrical field of ECG. The strain sensor consists of a sandwiched piezoresistive CNT-PDMS strip for sensing and two thin layers of flexible PDMS polymer for isolation. The ECG electrodes are placed in the minimum strain area on the substrate. Experimental data show that the interference between the mechanical deformation of the skin and the electrical field of ECG could be effectively eliminated in the captured signals in the proposed device design.

2. Results and discussions

The key challenge in wearable devices for personalized healthcare is simultaneously measurement of multiple physiological activities due to the interference between these multiple physical signals [31]. In this study, a CNT-PDMS based device was developed to achieve simultaneous measurement of the ECG and wrist pulse pressure (Fig. 1A). The device integrates a strain-sensing element (a suspended PDMS membrane embedded with CNT-PDMS strip) and voltage-sensing element (CNT-PDMS electrodes). The layout of sensing elements in the device was guided by the simulation of the strain distribution and the electrical field distribution, which minimized the interference between the wrist pulse and cardiac electric activity during measurement. Each sensor was preconditioned under the strain of 20% until the resistance change of the strain-sensing element in the device reached a stable value. Based on the stabilized piezoresistive and voltage-sensing output, the device was able to perform simultaneous measurement of wrist pulse pressure and ECG signal at the human wrist.

2.1. Electrical field simulation and strain simulation

The layout of the sensing elements (CNT-PDMS electrode and piezoresistive CNT-PDMS strip) in the device was optimized by FEA. In the simulation model, the distance between the device and the skin was set to be 13.3 μm (see details in Section 2.3), which was experimentally measured by super-depth-of-field microscopy (Hitachi, Japan). In the simulation of the electrical field distribution, the amplitude of the ECG signal was set to be 1.2 mV according to the result given in the literature [32]. As shown in (Fig. 1B and C), the simulation results showed that the potential was decreased to 0.45 mV on the CNT-PDMS ECG electrode with a sensing range of 2 mm above the ECG signal source on the skin. The amplitude of ECG would decrease by about 62.5% during transmission through the air gap to the electrode.

During each heartbeat, a wrist pulse travels along the linear ulnar artery in the human carpal branch, which generates a pressure change in the artery. Therefore, the pressure in the simulation model was applied along the orientation of the CNT-PDMS strain sensor. Wrist pulse pressure is typically 1.05 kPa ± 0.27 kPa [33]; thus, we used it to simulate the strain distribution of the suspended membrane caused by wrist pulse. The Young's modulus of the suspended PDMS membrane was set to be 467.5 kPa ± 10.27 kPa (n = 6), which was experimentally measured by AFM indentation. The simulation result showed that the stress gradually decreased from the top center to the bottom edge. The corresponding stress values decreased from 513 Pa to 421 Pa (see Fig. 1D). The result revealed that wrist pulse pressure could be measured by the resistance change of the CNT- PDMS strain sensor due to the strain change in the suspended membrane. In addition, the deformation of the membrane was within 3 mm along the orientation of the applied pressure. The simulation results above revealed that ECG measurement would not be disturbed when the distance between the CNT-PDMS electrode and the strain sensor was larger than 3 mm, which proved the effectiveness of the layout of the device in eliminating the interference between the ECG and the wrist pulse signals.

2.2. Device characterization results

2.2.1. Device profiler

To characterize the geometric features of the device, the height profile of the device surface was measured by an optical profiler (LS-K 3D, Brucker, USA) after each step of the fabrication process (see details in methods Section 3.2). As shown in Fig. 1E, the height of the ECG substrate was 472 μm ± 17 μm, the thickness of the suspended membrane was 68 μm ± 11 μm. CNT-PDMS strain sensor has a width of 2.3 mm ± 0.31 mm and a thickness of 50 μm ± 6.3 μm. The top PDMS layer has a thickness of 42.0 μm ± 4.9 μm.

2.2.2. XRD profile for composite material analysis

XRD was used to determine the existence of CNT and PDMS. The XRD diffraction pattern result was shown in Fig. 1F. The black curve (PDMS) sample contains two peaks: the first one at around $2\theta = 12.1^{\circ}$ and the second broader one from 16.7° to 30.3°, which agreed with the XRD profiles of PDMS previously obtained in literature [34]. In the red curve (CNT-PDMS), two similar peaks appeared at the same 2θ angles, which matched the XRD profiles of PDMS in our black curve. This indicated the presence of PDMS. In addition, several peaks appeared at

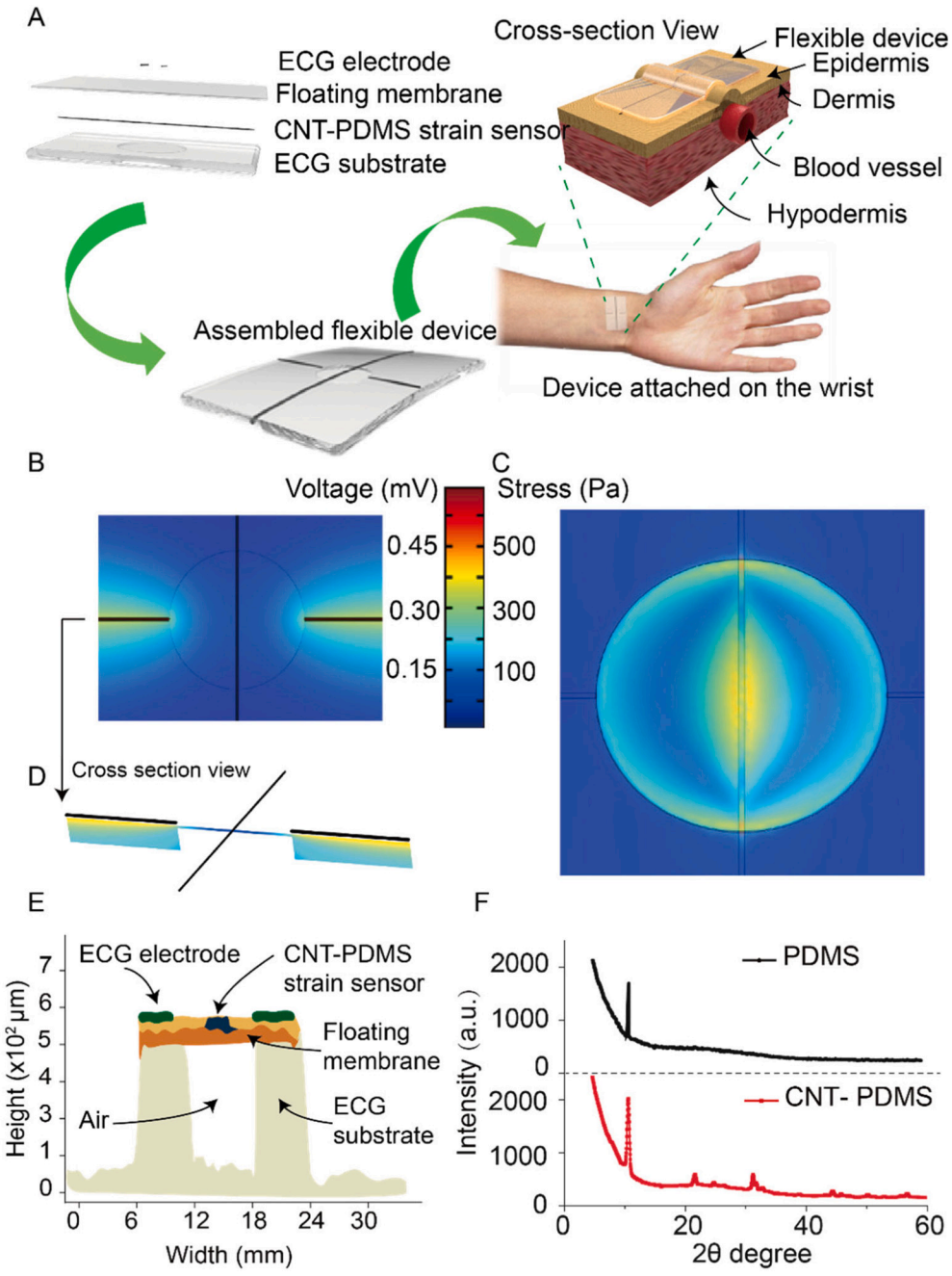

Fig. 1. (A) Schematic of the CNT-PDMS wearable device structure for measurement of wrist pulse pressure and ECG. The ECG signal was captured by the flexible CNT-PDMS ECG electrodes. The shape change of blood vessels during a wrist pulse induced the resistance change of the CNT-PDMS strain sensor. (B) Simulation result of the electrical field distribution around the ECG electrodes when a voltage (1.2 mV) used as a signal source was applied on a plane (corresponding to the human skin surface) 13.3 μm above the ECG electrodes. (C) Simulation result of the strain distribution on the floating membrane caused by a wrist pulse. The applied pressure of the wrist pulse was 1.05 kPa. The strain gradually decreased from the center (513 Pa) to the edge (421 Pa) on the floating membrane. (D) The cross-section view of the electrical field distribution around the ECG electrodes in (B). (E) The dimension of the cross-section at the sensing region in the device, which was measured by optical profiler during each step of device fabrication. The thickness of the CNT-PDMS strip was 50 μm. The thickness of the suspended PDMS membrane was 200 μm. (F) The XRD spectra of PDMS and CNT-PDMS composites. The first peak of PDMS (black curve) appears at around 2θ = 12.1° and the second broader peak appears from 16.7° to 30.3°. Peaks in the red curve of the CNT-PDMS XRD profile appear at the 2θ degree of 22.0°, 32.0°, and 45.0° confirming the presence of CNT. (For interpretation of the references to colour in this figure legend, the reader is referred to the web version of this article.)

2θ = 22°, 32° and 45°. The diffraction peak at around 2θ = 22° corresponded to the C (002) of the graphite structure in CNT inside the CNT-PDMS composite [35,36].

2.2.3. Preconditioning of the wearable device

A customized stretching instrument was used to periodically stretch and release the CNT-PDMS material during the preconditioning process, as shown in Fig. S2A and Supplementary Video 1). The inset in Fig. 2A showed that a CNT-PDMS device was periodically stretched. Red dashed and solid lines respectively were the outlines of the suspended PDMS membrane at the initial state and under the strain of 20%. Fig. S2B showed the resistance (R) of a fresh-fabricated device during the preconditioning process for over 9.7 h. After preconditioning over 3.8 h, the resistance of the device trended to be stable, indicating that the internal conductive network structure trends to be stabilized. To avoid the problem of the resistance difference among devices due to fabrication and assembly errors, the relative resistance change ($\Delta R/R_0$) was introduced to normalize the resistance changes. Fig. 2A showed $\Delta R/R_0$ of 6 devices increased during the process of preconditioning and stabilized at the value of 0.05 ± 0.002. To explore the reason for the above phenomenon, the morphologies of CNT-PDMS were determined by SEM before and after preconditioning (see the details in Section 2.3).

In addition, the hysteresis curves of the CNT-PDMS wearable device was shown in Fig. S7. Although the resistance change for strain improved along the orientation of the strain, and the hysteresis of the CNT-PDMS exists during loading and unloading of the strain. However, the hysteresis has no significant difference before and after preconditioning process.

The reason for the existing of hysteresis is that the hysteretic resistance is governed by a microstructural parameter ξ (the ratio of the mean projected CNT length over the film length) and ξ is hysteretic with strain and that the resistance is proportional to ξ^{-2} [1–3].

No difference of hysteresis was observed before and after preconditioning process. This is because that the hysteresis of the CNT-

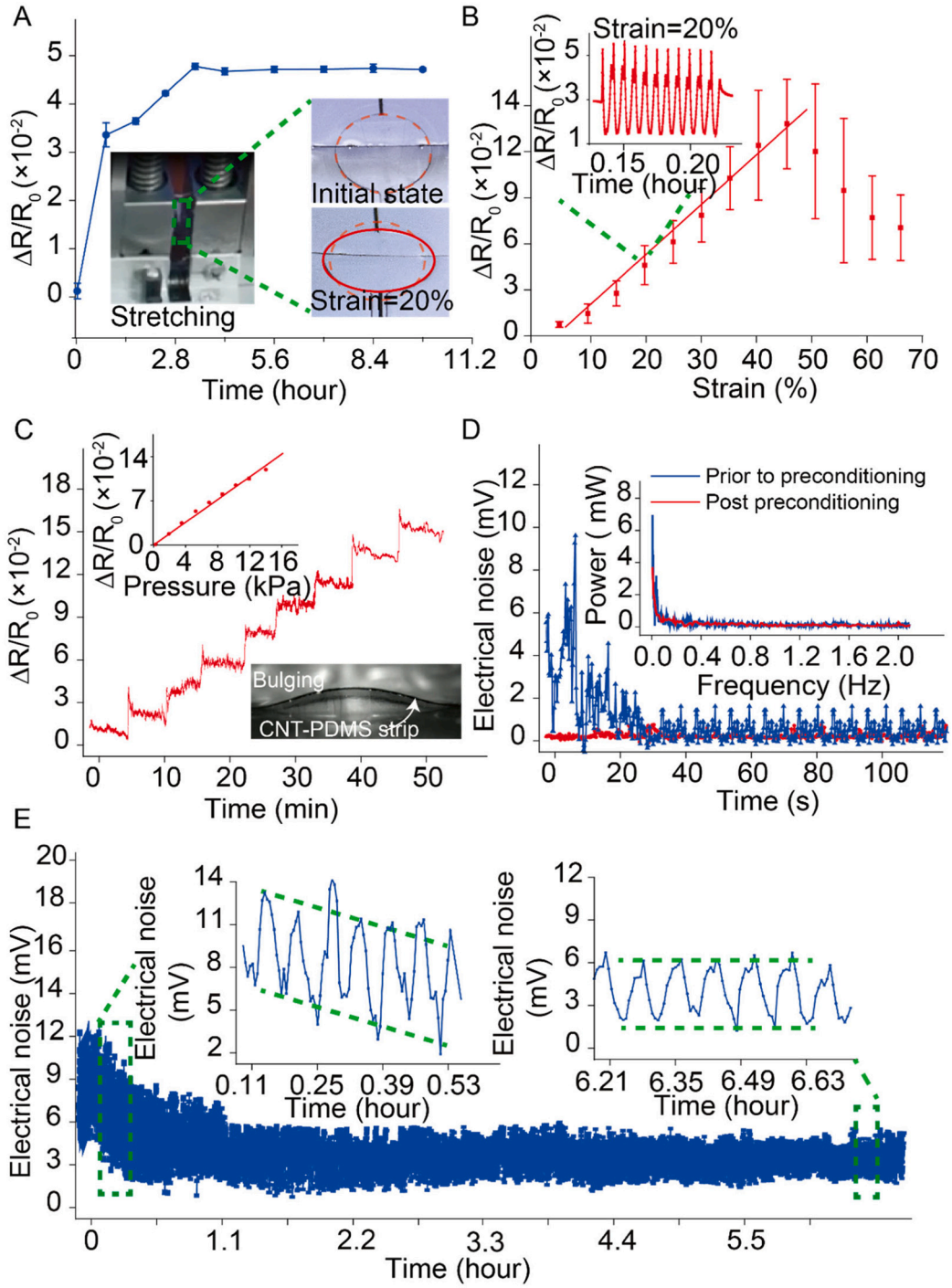

Fig. 2. Characterization of the mechanical and electrical properties of the proposed device. (A) Resistance change ($\Delta R/R_0$) during preconditioning showed at the bottom left inset. The bottom-right inset shows the shape change of the suspended membrane under the strain of 20% using the customized stretching instrument. (B) The repeating tensile testing of the device by the applied strain from 5% to 65%. The resistance change ($\Delta R/R_0$) of the strain sensor was recorded. The relationship between $\Delta R/R_0$ and the applied strain was linear in the strain range of up to 45%. (C) Calibration of the relationship between $\Delta R/R_0$ and pressure after preconditioning, which can be used to calculate the piezoresistive sensitivity of the strain sensor. The bottom-right inset shows the device bulged under 20% strain. (D) The noise level of the CNT-PDMS electrode before and after preconditioning. The noise level of the sensor reduced from 2.1 mV ± 0.39 mV to 237 μV ± 29 μV after the preconditioning process. The inset shows the frequency spectrum of the noise before and after preconditioning. (E) The reduction trend of the noise level in the CNT-PDMS electrode during preconditioning. The pre-conditioning process could stabilize the internal structure of the CNT network.

PDMS composite was mainly caused by the viscoelasticity property of the polymer (PDMS). The preconditioning process was performed within the range of elastic response (the value for this is 0.42 under the cyclic strain of 5%).

2.2.4. Tensile testing result of the wearable device

After preconditioning, tensile testing was performed to find out the linear range of the strain for the device. Three samples were tested by applying an external strain from 5% to 65%. Each stretching process was repeated ten times. The corresponding resistance was recorded. The inset in the top-left of Fig. 2B showed the $\Delta R/R_0$ changed with time under the strain of 20%. Fig. 2B showed that $|\Delta R/R_0|$ linearly increased with the increment of the strain (5% to 45%). The fitted linear curve has a correlation coefficient of 0.98. The yield point occurred at strain = 45%, after that, the $\Delta R/R_0$ decreased although the strain increased. The adjacent CNT loses connection with each other when the strain exceeds 45%. After the strain was released, the CNTs were unable to recover the initial position. The static resistance (R_0) was increased due to the yield strain, which means the original CNT inter-connection network was broken down. As a result, the relative resistance change ($\Delta R/R_0$) decreased.

2.2.5. Calibration result between $\Delta R/R_0$ and pressure

For accurately predicting wrist pulse pressure using the developed device, the relationship between resistance change ($\Delta R/R_0$) and the pressure was first calibrated. To this end, signals of resistance and

pressure were simultaneously recorded when different magnitudes of pressure were used to bulge the strain sensor (suspended membrane with CNT-PDMS strip) in the device. The pressure was produced by a customized syringe pump and a device was sealed onto a cylindrical PDMS. The pressure changed from 0.4 kPa to 14.0 kPa. The corresponding $\Delta R/R_0$ stepwise increased from 0.0035 to 0.15 (Fig. 2C). The curve of $\Delta R/R_0$ vs. pressure was recorded and fitted into a linear curve, as shown in the inset of Fig. 2C. The calculated sensitivity for the pressure measurement was 0.01 Pa^{-1}. The linearity range of the CNT-PDMS strain sensor covered the whole range from 0.4 kPa to 14.0 kPa.

2.2.6. Characterization result for the electrical properties of the ECG electrode

To stabilize the ECG reading, the CNT-PDMS electrode was also preconditioned by stretching under the strain of 20% periodically. To characterize the electrical signal capturing performance after preconditioning, the static noise was measured continuously for 120 s, as shown in the red curve in Fig. 2D. The peak-to-peak value of the electrode noise after preconditioning decreased to 18% compared to that before preconditioning (the blue curve in Fig. 2D). Fourier transform was used to analyze the power density spectrum of the noise. The first peak was observed at 2 Hz and its magnitude decreased about twice after preconditioning. Fig. 2E showed that the amplitude of noise decreased to 11% of that before preconditioning for 6.2 h (237 μV ± 29 μV vs. 2.1 mV ± 0.39 mV).

2.3. Mechanisms of CNT-PDMS strip for measuring ECG and wrist pulse pressure

To explore the working mechanisms of measuring ECG and wrist pulse pressure in the proposed device, the morphologies of CNT-PDMS composites and the equivalent circuit model of the ECG sensing element were investigated.

To investigate the underlying mechanism of how ECG signals were captured by the CNT-PDMS electrodes, an equivalent circuit model was proposed for decoupling the connections in the skin-CNT-PDMS electrodes. The impedance spectra of CNT electrodes, pigskin, and the combination of CNT-PDMS electrodes and pigskin were measured from 0.1 Hz to 100 kHz. Nyquist plot and Bode plot were adopted to analyze the impedance results [37], which were commonly used for decoupling each electrical element in the equivalent circuit model [38]. Due to pigskin's morphology and physiology were similar to human skin [39], pigskin was attached to the wearable device (see Fig. 3A and B). As shown in the black points in Fig. 3C and D, the frequency response of CNT-PDMS was a constant value (643 Ω) that did not change with the increase of frequency in the Bode plot, and the frequency response of CNT-PDMS in Nyquist plot was many points around the coordinate (643 Ω, 0). These results revealed that CNT-PDMS element could be regarded as a resistor (R_0 in Fig. 3B). The frequency response of pigskin was a line with the slope of 0.45 in the Nyquist plot in the red points of Fig. 3C and D, which was suitable for the response of a constant phase element (CPE in Fig. 3B). The CPE constant was 90 nF and the exponent of the CPE was 0.63. Finally, the overall equal circuit model can be established through measuring the frequency response of the device attached onto the pigskin surface. A semi-circle appeared in the frequency response curve (blue curves in Fig. 3C and D), which was due to the double layer capacitor formed by the gap between pigskin and wearable device. This kind of response is the result of the parallel connection of a resistor (17.8 kΩ) and a capacitor (90 nF).

To explore the piezoresistive mechanism of the CNT-PDMS strain sensor, the SEM morphologies of the CNT-PDMS composite before and after the preconditioning process were captured as shown in Fig. 3E and F. The pool regions were marked with a red dashed circle. The statistic results of the pool area in Fig. S3 revealed that the pools could be classified into small and large groups according to the area. The ratio between large pools (area $>$ 300 μm^2) small pools (area $\leq$ 300 μm^2) was increased from 0.26 to 0.50, which indicated that a portion of small pools was broken into large pools during preconditioning. This was consistent with CNT-PDMS the literature that during preconditioning small CNT-PDMS pools were broken into larger CNT-PDMS pools [40]. The potential explanation in microscale was: The resistance of CNT-PDMS composite is determined by the quantum tunneling effect between adjacent CNTs (distance $<$ 10 nm) [41,42], and the conductive path formed by the inter-connections of CNTs [43]. When an external force is applied on the composite, the distance between the adjacent CNTs becomes larger, the formed CNT conductive path could be destroyed if the distance is larger than 10 nm. Accordingly, the chance of electronic transition between adjacent CNTs is reduced. In addition, the elastic modulus of the PDMS is much smaller than CNT (0.85 GPa vs. 34.5 GPa) [44]. Under the same tensile strain, the strain of PDMS is much larger than that of CNT. As a result, a shearing force is generated between CNT and PDMS, which breaks the inter-connections between the adjacent CNTs. From the macroscale view, the resistance of the CNT-PDMS sensor would be increased under external stretch. CNT-PDMS composites under external force, the connections among CNTs would break, and the relative position of CNT rearranged, leading to the overlapped region among CNTs disappear or reform. As a result, the corresponding $\Delta R/R_0$ caused by the same strain during preconditioning tended to increase, as shown in Fig. S2B, which indicated that the sensitivity of the CNT-PDMS strain sensor was increased by the preconditioning process and finally stabilized. In addition, the static resistance of the CNT-PDMS strain sensor in Fig. S2B tended to decrease during the preconditioning process due to the conductive network in the CNT-PDMS tends to be regular and stable [45].

2.4. Simultaneous recordings of ECG and wrist pulse pressure

To demonstrate the performance of the proposed device, 9 volunteers (five males, four females, and ages from 18 to 20) were measured for monitoring wrist pulse pressure and ECG. The devices were attached to the surface of the right-hand wrist (Fig. S6 and Supplementary Video 2), and holders were used to connecting the device and testing equipment. The signals from the volunteers were recorded for 1 min at rest and after running for 500 m. Fig. 4A showed the ECG signals of a volunteer before and after exercise. Under resting state, ECG signals were regular waves with a beating period of 0.83 s ± 0.11 s in the time-domain plot. Fig. 4B was the enlarged plot during the time from 35 s to 40 s, showing that the amplitude of the ECG was 276 μV ± 31 μV. The right plot in Fig. 4A was the ECG signal obtained 1 min post running. The beating period of wrist pulse decreased to 0.45 s ± 0.17 s. The amplitude of the ECG signal has no significant difference compared to that under resting state. Poincaré plot was commonly used to evaluate heart arrhythmia in the medical analysis [46], here we employ it to analyze the ECG signal. Fig. 4C shows that the center point of the signal distribution focus around the point (0.83 s, 0.83 s); however, after exercise the center point of the signal distribution focus around the point (0.45 s, 0.45 s). In addition, we noted that the cloud of the points became larger, demonstrating wrist pulse became irregular, which reflects heart arrhythmia after volunteer running. In addition, the wrist pulse pressure signals were simultaneously measured along with ECG. The signals at rest and post running were captured in Fig. 4D. At rest, the wrist pulse has a regular rhythm, whose amplitude was 485 Pa ± 23 Pa. However, the amplitude of the wrist pulse increased to 504 Pa ± 41 Pa. For better comparison, the details of the wrist pulse were enlarged to show in Fig. 4E. Fourier transform was used to compare pulse frequency distribution before and after running (Fig. 4F). The main frequency of wrist pulse has moved from 1.2 Hz to 2.24 Hz, whose change resembled with the change of ECG frequency. From the results above, our device could provide six parameters for evaluating health conditions at the same time, including beating frequency, beating rhythm, and beating amplitude from ECG, and pulse frequency, pulse rhythm, and pulse amplitude from wrist pulse wave. In addition,

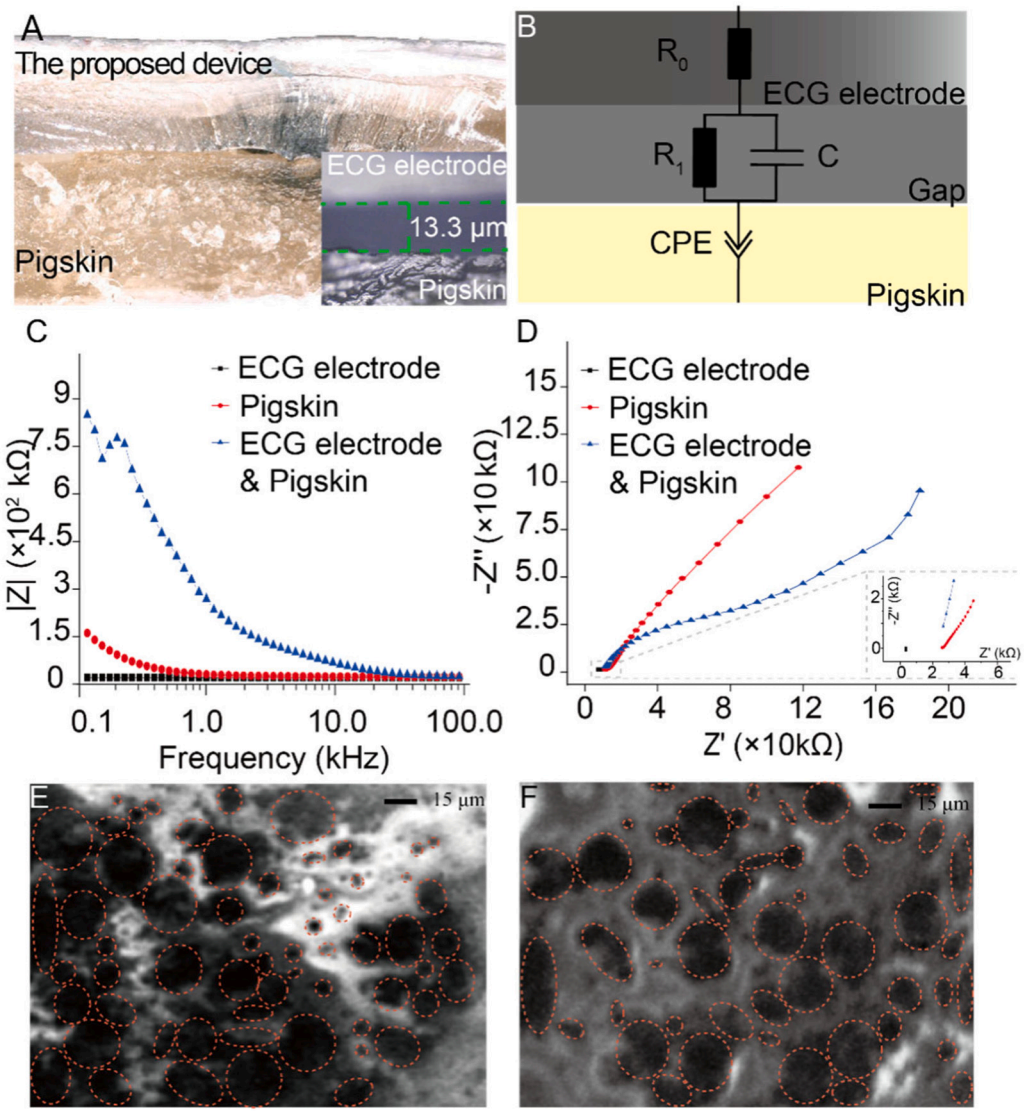

Fig. 3. Sensing mechanisms of CNT-PDMS strip for measuring ECG and wrist pulse pressure. (A) The experiment setup for ECG measurement. The proposed device was attached to a piece of pigskin. The distance between the bottom PDMS layer to the pigskin is about 13.3 μm according to the optical image result. (B) A circuit model for the electric connection between the device and the pigskin. In the circuit model, R_0 represents the ECG electrode. R_1 and C represent the gap between the ECG electrode and the pigskin. CPE represents the pigskin. (C) and (D) The Bode plots and the Nyquist plots for the device measured by an electrochemical workstation. The inset in (D) is the enlarged view of the rectangular region for showing the frequency response of CNT-PDMS, which showed that the CNT-PDMS electrode can be considered as a resistor (R_0 = 643 Ω). (E) and (F) The surface morphology of CNT-PDMS composites captured by SEM before and after preconditioning. After preconditioning, the pool structures (CNT clusters) in the CNT-PDMS material became more uniform. The ratio between the large pools (area > 300 μm^2) and the small pools (area ≤ 300 μm^2) was increased from 0.26 to 0.50 possibly due to a portion of small pools was broken and changed to large pools during preconditioning.

the recovering process of the ECG and wrist pulse waveform after exercise for 1.25 h was recorded as shown in Fig. S4. The results demonstrated that our device could be used for long-term (> 1 h) monitoring of personal health conditions.

In addition, we have compared our results with that of the commercial ECG electrodes (the disposable Ag/AgCl ECG electrode, Xunda wireless electronics Inc. Hangzhou, China). The data are plotted in Fig. S5. Our result is comparable with the conventional ECG sensor in terms of beating frequency and beating rhythm. The wrist pulse results obtained from our proposed strain sensor were also compared with that obtained from the commercial piezoresistive wrist pulse sensor (RFP602, Yubo Intelligent Technology Co. Ltd. Hangzhou, China).

3. Methods

3.1. Device design and fabrication

To solve the interference between the mechanical deformation of the skin and the electrical field of ECG in the sensor, the following optimal sensor design methods were proposed. The thickness of the substrate membrane for the pulse strain sensor should be minimized to improve the sensitivity. In the meanwhile, the substrate thickness for the ECG electrode should be thick enough to avoid the electrode-skin contact distance changes due to the mechanical deformation of the skin. Therefore, the device design contains the ECG substrate, the suspended membrane for pulse sensing, the CNT-PDMS strain sensor, and the thick ECG substrate. The steps involved in the fabrication of the CNT-PDMS device are shown in Fig. S1.

(a) ECG substrate

An aluminum mold was designed as shown in Fig. S1G. 96 pillars (height = 450 μm, diameter = 4.14 mm) were distributed evenly. A mixture of the PDMS curing agent and the base PDMS polymer (weight ratio = 1:10) was poured into the mold and baked at 65 °C for 4 h. After solidification and peeling off, cavities were formed on the PDMS substrate due to the pillars, which would be used to suspend the membrane fabricated in the next step.

(b) Suspended membrane

To increase the stickiness and flexibility of the suspended membrane, the weight ratio of the PDMS curing agent and the base PDMS polymer was set to 1:20. Then the PDMS mixture was spin-coated on an acrylic board. Considering the fabrication success rate and optimal sensitivity of the pulse sensor, the speed of spin-coating for the PDMS mixture was selected as 750 r/min. This resulted in an 85 μm suspended membrane after solidification. The coated acrylic board was then baked

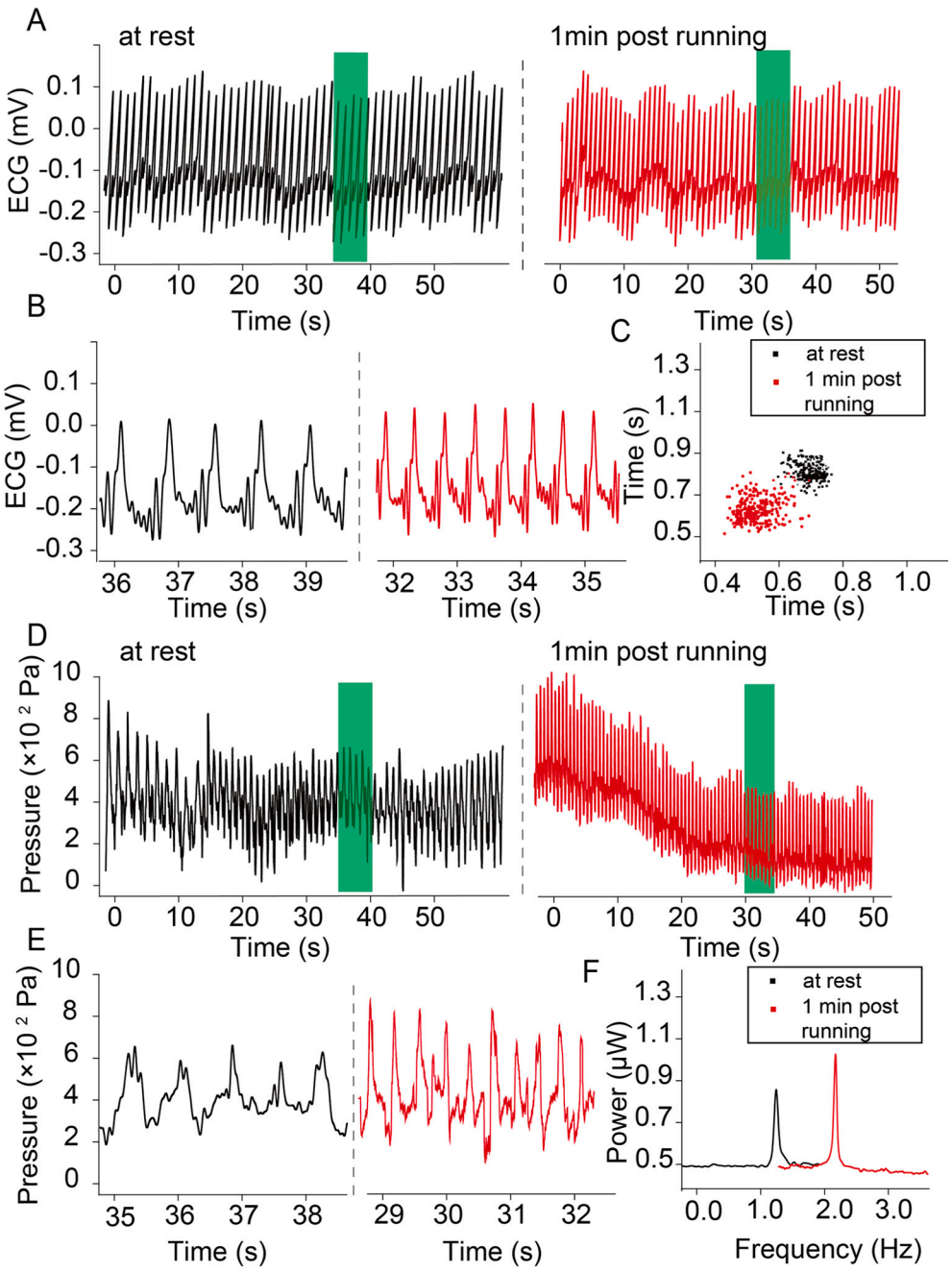

Fig. 4. The measurement of ECG and wrist pulse for a volunteer before and after running. (A) ECG signal captured from a volunteer at rest and after running. (B) Enlarged view of the ECG signals in the green region in (A). (C) Poincaré plot for the ECG signal at rest and after running. At rest, the center point of the signal distribution focuses around the point (0.83 s, 0.83 s); however, after exercise the center point of the signal distribution focus around the point (0.45 s, 0.45 s). In addition, the diameter of the point cloud became larger, which reflects heart arrhythmia after volunteer running. (D) Wrist pulse pressure captured from a volunteer at rest and after running. (E) Enlarged view of wrist pulse pressure in the green region in (D). (F) The frequency spectrum of the ECG signals at rest and after running. The beating frequency and amplitude of the ECG and wrist pulse signals after running were increased compared to that of the rest state. (For interpretation of the references to colour in this figure legend, the reader is referred to the web version of this article.)

at a temperature of 65 °C for 4 h. After solidification, a thin film was formed and then peeled off from the acrylic board. Finally, the thin PDMS film was assembled onto the ECG substrate. The film was suspended in the cavity region of the ECG substrate.

(c) CNT-PDMS strain sensor

Multi-walled carbon nanotubes (CNT) and PDMS were (weight ratio = 1:25) were mixed together and blended. The CNT-PDMS blends were uniformly painted on the surface of the suspended region on the film to form a sensor strip (width = 300 μm) by using the screen printing method. Then the whole device was baked at 65 °C for 4 h. After solidification, the CNT-PDMS sensor strip is 50 μm thick. When an external force was applied on the sensor strip, the polymer substrate would deflect, which resulted in a change in the inner-network of CNT and induced the change in resistance. In order to isolate the disturbance of the electrical cardio pulse in strain measurement, another layer of PDMS insulating film was fabricated on top of the CNT-PDMS strain sensor.

(d) ECG electrode

Two CNT-PDMS electrodes were screened on the top of the PDMS insulating film, as shown in Fig. S1F. Then the whole device was baked at 65 °C for 4 h. The benefit of this design is that electrodes would directly adhere to the skin surface because PDMS is highly bio-compatible, which maximized the ECG capturing ability [47]. In addition, the ECG electrodes were arranged in the thick region of the ECG substrate, which minimizes the internal resistance change of ECG electrodes caused by the mechanical deformation of the skin when wrist pulses arrived.

3.2. Optical profiler and SEM

To obtain dimension detail of the device, an optical profiler (Bruker, USA) was used to test during each step in the process of preparation. First, the intermediate focusing-speed mode was used to find the interfering fringe. Then, the slow focusing-speed mode was to regulate the clarity of the interfering fringe. Finally, the knob under the objective stage was used to adjust the number of the interfering fringe. SEM was used to characterize the surface morphologies of CNT-PDMS.

3.3. XRD analysis

X-ray diffraction (XRD) of PDMS and CNT/PDMS were measured using an X-ray diffractometer (Rigaku, model Geigerflex) at the room temperature (25 °C). The diffractograms were measured at a scanning speed of 8° min^{-1}, by means of a tube voltage of 40 kV and tube current of 30 mA.

3.4. Finite element analysis (FEA)

The layout of the wearable device was optimized by FEA, whose simulation result would help to determine the distance between the microelectrodes and the strain sensor in the device. Input data including elastic modulus of PDMS and CNT-PDMS, dimensions of the device and the applied pressure is necessary for obtaining accurate simulation. Their values were measured by Atomic Force Microscopy (AFM, Bruker, America) and optical profiler. PDMS was commonly regarded as the isotropic elastic material, and 0.49 was used as its poison's ratio in the simulation model [48]. The applied pressure was 1.05 kPa.

To determine whether ECG affects the detection of the wrist pulse pressure, the electric field distribution of ECG was simulated. According to the reported reference, 1.2 mV ± 0.3 mV [32]. The conductivity of the CNT-PDMS electrode is defined as 106 S/m, which relative dielectric constant is 12. The main material in this device was PDMS, and its conductivity was defined as 10^{-3} S/m. The other properties were used the default values in the software.

3.5. Preconditioning device

As the relaxation effect exists in CNT-PDMS composites [49], a preconditioning process was applied by stretching and relaxing the CNT-PDMS material revealingly, which can stabilize the internal CNT network. The preconditioning process for each new device lasted for over 9.7 h. This way could contribute to sense pressure and ECG with accurate and stable sensitivity, linear range, detection limitation, and bio-electrical signal. For the preconditioning wearable device, we developed a home-made stretching instrument. This instrument was constructed by three parts, including the control component, transmission component, and clamping device. Control components consist of the control panel, the power, and the source drive. The transmission component is used to precisely regulate the movement of the ball screw, which includes a motor, a screw, a guide rail, and a sliding table. The clamping device is mainly used for fixing the flexible device during the preconditioning process. When the stretching instrument works, it controls the ball screw with linear motion back and forth, through regulating the control panel input program.

3.6. Calibration of CNT-sensing devices

A diaphragm pump (Schwarzer, model SP 500EC) and a programmable pressure regulator (Marsh Bellofram, model 3420) was used to deliver pressure, P, into the device channels through a single inlet. In-house electronics and LabView scripts were used to regulate P and to monitor the strain sensors' electrical resistance at a sampling rate of 10 Hz. For strain sensing, a fixed voltage of 2.5 V was applied to each sensor and the electrical current was monitored using a precision multichannel impedance analyzer. The sensors were preconditioned using a minimum of 4000 s. During calibration, using a cyclic driving pressure with different magnitudes, the peak-to-peak amplitude of the resistive strain of the sensors remained constant and was recorded to correlate with the amplitude of free bulging height of the membrane.

3.7. Measurement configuration

To achieve simultaneous measurement of wrist pulse and ECG record resistance and voltage. The Wheatstone bridge was used to measure the resistance of the wrist pulse sensor. A bandpass filter (0.5 Hz–10 Hz) was used to exclude the noise. The sampling rate for resistance measurement was set to 10 kHz. For ECG measurement, the CNT-PDMS ECG electrode was connected to the data acquisition board with the same sampling rate of 10 kHz. The recorded signals were filtered in the range of 0.5 Hz–10 Hz.

3.8. Monitoring volunteers' wrist pulse pressure and ECG

After device characterization, wrist pulse pressure and ECG measurement were conducted on 9 volunteers. A premise source meter (Keithley, model 2602) and high-speed electrical board were used to record resistance changes and ECG of the CNT sensors before and after volunteers exercise. Amperometric measurements were performed at a sampling rate of 1 kHz and the voltage across the CNT-PDMS sensor was maintained at 0.25 V. Voltage measurements were performed at a sampling rate of 30 kHz.

4. Conclusion

In this paper, a wearable device was developed that can simultaneously measure wrist pulse pressure and ECG signals. The challenge of the interference between the wrist pulse and ECG was solved by an optimized sensor layout. The bio-compatible CNT-PDMS composite was fabricated into a strain sensor to measure the wrist pulse pressure and flexible electrodes to capture the ECG signal. The sensor layout was optimized by finite element analysis. A preconditioning process (periodically stretching up to 20% strain) was performed to stabilize the output of the wrist pulse and ECG sensors. The relationship between the resistance change and the pressure was calibrated in the pressure range from 0.4 kPa to 14.0 kPa, and the calibrated sensitivity was 0.01 Pa^{-1}. SEM imaging and equal circuit modeling were employed to explore the mechanisms of CNT-PDMS for strain and electrical sensing. The proposed device was applied to monitor the wrist pulse and ECG signals of volunteers during the recovering process after physical exercises. Next step, wireless communication (e.g. Bluetooth) would be used to transmit the data captured by the device to a mobile phone for wireless monitoring. The data would be sent from the mobile phone to the server and analyzed to provide early warnings of cardiac diseases.

Supplementary data to this article can be found online at https://doi.org/10.1016/j.msec.2020.111345.

CRediT authorship contribution statement

Conceptualization, Jun Chen, Chonghai Xu, Yu Sun, and Li Wang; methodology, Li Wang. and Wenkun Dou; software, Kechao Lu and Feng Zhang; validation, Mohammed Abdulaziz; formal analysis, Weiguang Su; investigation, Anqing Li; resources, Li Wang; data curation, Li Wang, Jun Chen; writing—original draft preparation,Li Wang; writing—review and editing, Jun Chen, Chonghai Xu, Yu Sun, and Li Wang; project administration, Jun Chen, Chonghai Xu, Yu Sun; funding acquisition, Jun Chen, Chonghai Xu, Yu Sun.

Declaration of competing interest

We declare that we have no financial and personal relationships with other people or organizations that can inappropriately influence our work, there is no professional or other personal interest of any nature or kind in any product, service and/or company that could be construed as influencing the position presented in, or the review of, the manuscript entitled.

Acknowledgment

The authors acknowledge the financial support from the National Natural Science Foundation of China (Grant No. 61901239, 51908299), the Taishan Scholars Program of Shandong Province (NO.tsqn201812087), and the Major Science and Technology Innovation Projects of Shandong Province (Grant No. 2019JZZY010731). Li Wang would like to acknowledge the guidance from his postdoctoral advisor Professor Yu Sun (University of Toronto) and his Ph. D. advisor Professor Xinxia Cai (Institute of Electronics, Chinese Academy of Sciences).

References

[1] F.M. Sacks, A.H. Lichtenstein, J.H.Y. Wu, L.J. Appel, M.A. Creager, P.M. Kris-Etherton, M. Miller, E.B. Rimm, L.L. Rudel, J.G. Robinson, N.J. Stone, L. V. Van Horn, Dietary fats and cardiovascular disease: a presidential advisory from the American Heart Association, Circulation. 136 (2017). doi:https://doi.org/10.1161/CIR.0000000000000510.

[2] A. Ahmed, S.A. Hannan, Data mining techniques to find out heart diseases : an overview, (Sem Qualis) Int, J. Innov. Technol. Explor. Eng. 1 (2012) 18–23.

[3] N. Ayache, D. Chapelle, F. Clément, Y. Coudière, H. Delingette, J.A. Désidéri, M. Sermesant, M. Sorine, J.M. Urquiza, Towards model-based estimation of the cardiac electro-mechanical activity from ECG signals and ultrasound images, in: 2001: pp. 120–127. doi:https://doi.org/10.1007/3-540-45572-8_17.

[4] E.M.C. Hillman, O. Bernus, E. Pease, M.B. Bouchard, A. Pertsov, Depth-resolved optical imaging of transmural electrical propagation in perfused heart, Opt. Express 15 (2007) 17827, https://doi.org/10.1364/OE.15.017827.

[5] S.D. Solomon, S. Zelenkofske, J.J.V. McMurray, P.V. Finn, E. Velazquez, G. Ertl, A. Harsanyi, J.L. Rouleau, A. Maggioni, L. Kober, H. White, F. Van de Werf, K. Pieper, R.M. Califf, M.A. Pfeffer, Sudden death in patients with myocardial infarction and left ventricular dysfunction, heart failure, or both, N. Engl. J. Med. 352 (2005) 2581–2588, https://doi.org/10.1056/NEJMoa043938.

[6] D. Ho, X. Zhao, S. Gao, C. Hong, D.E. Vatner, S.F. Vatner, Heart rate and electrocardiography monitoring in mice, Curr. Protoc. Mouse Biol. (2011) 123–139, https://doi.org/10.1002/9780470942390.mo100159.

[7] L. Sörnmo, P. Laguna, Electrocardiogram (ECG) signal processing, in: Wiley Encycl. Biomed. Eng., John Wiley & Sons, Inc., Hoboken, NJ, USA, 2006. doi:https://doi.org/10.1002/9780471740360.ebs1482.

[8] A. Deodhar, T. Dickfeld, G.W. Single, W.C. Hamilton, R.H. Thornton, C.T. Sofocleous, M. Maybody, M. Gónen, B. Rubinsky, S.B. Solomon, Irreversible electroporation near the heart: ventricular arrhythmias can be prevented with ECG synchronization, Am. J. Roentgenol. 196 (2011) W330–W335, https://doi.org/10.2214/AJR.10.4490.

[9] M.I. Owis, A.H. Abou-Zied, A.-B.M. Youssef, Y.M. Kadah, Study of features based on nonlinear dynamical modeling in ECG arrhythmia detection and classification, IEEE Trans. Biomed. Eng. 49 (2002) 733–736, https://doi.org/10.1109/TBME.2002.1010858.

[10] C. Taylor, R. Hobbs, Diagnosing heart failure – experience and 'best pathways,' Eur. Cardiol. Rev. 6 (2010) 10. doi:10.15420/ecr.2010.6.3.10.

[11] L. Xu, M.Q.-H. Meng, C. Shi, K. Wang, N. Li, Quantitative analyses of pulse images in traditional Chinese medicine, Med. Acupunct. 20 (2008) 175–189, https://doi.org/10.1089/acu.2008.0632.

[12] D. Zhang, W. Zuo, P. Wang, Generalized feature extraction for wrist pulse analysis: from 1-D time series to 2-D matrix, in: Comput. Pulse Signal Anal, Springer, Singapore, Singapore, 2018, pp. 169–189, https://doi.org/10.1007/978-981-10-4044-3_9.

[13] T.E. Applegate, Atrial arrhythmias, Prim. Care 27 (2000) 677–708, https://doi.org/10.1016/S0095-4543(05)70169-X.

[14] G.W. Dorn, J.D. Molkentin, Manipulating cardiac contractility in heart failure: data from mice and men, Circulation. 109 (2004) 150–158, https://doi.org/10.1161/01.CIR.0000111581.15521.F5.

[15] B.A. Borlaug, C.S.P. Lam, V.L. Roger, R.J. Rodeheffer, M.M. Redfield, Contractility and ventricular systolic stiffening in hypertensive heart disease, J. Am. Coll. Cardiol. 54 (2009) 410–418, https://doi.org/10.1016/j.jacc.2009.05.013.

[16] E. Nemati, M.J. Deen, T. Mondal, A wireless wearable ECG sensor for long-term applications, IEEE Commun. Mag. 50 (2012) 36–43, https://doi.org/10.1109/MCOM.2012.6122530.

[17] K. Hänsel, N. Wilde, H. Haddadi, A. Alomainy, Challenges with current wearable technology in monitoring health data and providing positive behavioural support, MOBIHEALTH 2015 - 5th EAI Int. Conf. Wirel. Mob. Commun. Healthc. - Transform. Healthc. through Innov. Mob. Wirel. Technol, (2015), https://doi.org/10.4108/eai.14-10-2015.2261601.

[18] W. Zeng, L. Shu, Q. Li, S. Chen, F. Wang, X.M. Tao, Fiber-based wearable electronics: a review of materials, fabrication, devices, and applications, Adv. Mater. 26 (2014) 5310–5336, https://doi.org/10.1002/adma.201400633.

[19] M.. Paridah, A. Moradbak, A.. Mohamed, F. Abdulwahab Taiwo Owolabi, M. Asniza, S.H. Abdul Khalid, We are IntechOpen, the world's leading publisher of Open Access books built by scientists, for scientists TOP 1%, Intech. i (2016) 13. doi:https://doi.org/10.5772/57353.

[20] N. Lu, C. Lu, S. Yang, J. Rogers, Highly sensitive skin-mountable strain gauges based entirely on elastomers, Adv. Funct. Mater. 22 (2012) 4044–4050, https://doi.org/10.1002/adfm.201200498.

[21] D. Dias, J.P.S. Cunha, Wearable health devices—vital sign monitoring, systems and technologies, Sensors (Switzerland). 18 (2018). doi:https://doi.org/10.3390/s18082414.

[22] Y. Liu, H. Wang, W. Zhao, M. Zhang, H. Qin, Y. Xie, Flexible, stretchable sensors for wearable health monitoring: Sensing mechanisms, materials, fabrication strategies and features, Sensors (Switzerland). 18 (2018). doi:https://doi.org/10.3390/s18020645.

[23] T. Yang, W. Wang, H. Zhang, X. Li, J. Shi, Y. He, Q.S. Zheng, Z. Li, H. Zhu, Tactile sensing system based on arrays of graphene woven microfabrics: electromechanical behavior and electronic skin application, ACS Nano 9 (2015) 10867–10875, https://doi.org/10.1021/acsnano.5b03851.

[24] J. Shi, L. Wang, Z. Dai, L. Zhao, M. Du, H. Li, Y. Fang, Multiscale hierarchical design of a flexible piezoresistive pressure sensor with high sensitivity and wide linearity range, Small. 14 (2018) 1–7, https://doi.org/10.1002/smll.201800819.

[25] S.M. Lee, H.J. Byeon, B.H. Kim, J. Lee, J.Y. Jeong, J.H. Lee, J.H. Moon, C. Park, H. Choi, S.H. Lee, K.H. Lee, Flexible and implantable capacitive microelectrode for bio-potential acquisition, Biochip J. 11 (2017) 153–163, https://doi.org/10.1007/s13206-017-1304-y.

[26] P.H. Charlton, T. Bonnici, L. Tarassenko, An assessment of algorithms to estimate respiratory rate from the electrocardiogram and photoplethysmogram, Physiol. Meas. 610 (n.d.) 610. doi:https://doi.org/10.1088/0967-3334/37/4/610.

[27] R. Angle, A.L.A. Lcaine, D.A.R. Omero, E.D.G. Il, P.A.L. Aguna, Electrocardiogram Derived Respiratory Rate from QRS Slopes 40 (2014) 2072–2083, https://doi.org/10.1007/s10439-014-1073-x.

[28] S.R. Passmore, B. Murphy, T.D. Lee, The origin, and application of somatosensory evoked potentials as a neurophysiological technique to investigate neuroplasticity, J. Can. Chiropr. Assoc. 58 (2014) 170–183.

[29] M. Valencia, M. Alegre, J. Iriarte, J. Artieda, High frequency oscillations in the somatosensory evoked potentials (SSEP's) are mainly due to phase-resetting phenomena, J. Neurosci. Methods 154 (2006) 142–148, https://doi.org/10.1016/j.jneumeth.2005.12.011.

[30] H. Gui, J. Liu, Latest Progresses in Developing Wearable Monitoring and Therapy Systems for Managing Chronic Diseases, (2018) 1–30.

[31] A.K. Yetisen, J.L. Martinez-Hurtado, B. Ünal, A. Khademhosseini, H. Butt, Wearables in medicine, Adv. Mater. 30 (2018). doi:https://doi.org/10.1002/adma.201706910.

[32] R. Guo, X. Sun, S. Yao, M. Duan, H. Wang, J. Liu, Semi-liquid-metal-(Ni-EGaIn)-based Ultraconformable Electronic Tattoo, 1900183 (2019) 1–11. doi:https://doi.org/10.1002/admt.201900183.

[33] B. Nie, R. Li, J.D. Brandt, T. Pan, Iontronic microdroplet array for flexible ultrasensitive tactile sensing, Lab Chip 14 (2014) 1107–1116, https://doi.org/10.1039/c3lc50994j.

[34] P. Ferreira, Á. Carvalho, T.R. Correia, B.P. Antunes, I.J. Correia, P. Alves, Functionalization of polydimethylsiloxane membranes to be used in the production of voice prostheses, Sci. Technol. Adv. Mater. 14 (2013) 55006, https://doi.org/10.1088/1468-6996/14/5/055006.

[35] H. Soleimani, Synthesis of carbon nanotubes for oil-water interfacial tension reduction, Oil Gas Res. 1 (2015). doi:https://doi.org/10.4172/2472-0518.1000104.

[36] N.O. Ramoraswi, P.G. Ndungu, Photo-catalytic properties of TiO2 supported on MWCNTs, SBA-15 and silica-coated MWCNTs nanocomposites, Nanoscale Res. Lett. 10 (2015) 427, https://doi.org/10.1186/s11671-015-1137-3.

[37] R. Breaker, R. Penchovsky, Computational Design of Ribozymes (2008) 1–87 (doi:US20110288826).

[38] B. Archambeault, A.E. Ruehli, Analysis of power/ground-plane EMI decoupling equivalent circuit technique, IEEE Trans. Electromagn. Compat. 43 (2001) 437–445.

[39] E.C. Jung, H.I. Maibach, Topical drug bioavailability, bioequivalence and penetration, Gen. Pharmacol. Vasc. Syst. 26 (1995) 442, https://doi.org/10.1016/0306-3623(95)90008-x.

[40] C.S. Boland, U. Khan, G. Ryan, S. Barwich, R. Charifou, A. Harvey, C. Backes, Z. Li, M.S. Ferreira, M.E. Möbius, R.J. Young, J.N. Coleman, Sensitive electromechanical sensors using viscoelastic graphene-polymer nanocomposites, Science (80-.). 354 (2016). http://science.sciencemag.org/content/354/6317/1257.full (Accessed August 12, 2017).

[41] V. Skákalová, A.B. Kaiser, Y.-S. Woo, S. Roth, Electronic transport in carbon nanotubes: from individual nanotubes to thin and thick networks, Phys. Rev. B 74 (2006) 085403, , https://doi.org/10.1103/PhysRevB.74.085403.

[42] J.G. Simmons, Generalized formula for the electric tunnel effect between similar electrodes separated by a thin insulating film, J. Appl. Phys. 34 (1963) 1793–1803, https://doi.org/10.1063/1.1702682.

[43] W. Bauhofer, J.Z. Kovacs, A review and analysis of electrical percolation in carbon nanotube polymer composites, Compos. Sci. Technol. 69 (2009) 1486–1498,

https://doi.org/10.1016/j.compscitech.2008.06.018.
[44] L. Bokobza, Multiwall carbon nanotube elastomeric composites: a review, Polymer (Guildf). 48 (2007) 4907–4920, https://doi.org/10.1016/j.polymer.2007.06.046.
[45] Y. Yu, Y. Luo, A. Guo, L. Yan, Y. Wu, K. Jiang, Q. Li, S. Fan, J. Wang, Flexible and transparent strain sensors based on super-aligned carbon nanotube films, Nanoscale. 9 (2017) 6716–6723, https://doi.org/10.1039/c6nr09961k.
[46] P. Guzik, J. Piskorski, T. Krauze, R. Schneider, K.H. Wesseling, A. Wykrętowicz, H. Wysocki, Correlations between the Poincaré plot and conventional heart rate variability parameters assessed during paced breathing, J. Physiol. Sci. 57 (2007) 63–71, https://doi.org/10.2170/physiolsci.RP005506.
[47] L. Guo, G.S. Guvanasen, X. Liu, C. Tuthill, T.R. Nichols, S.P. Deweerth, A PDMS-based integrated stretchable microelectrode array (isMEA) for neural and muscular surface interfacing, IEEE Trans. Biomed. Circuits Syst. 7 (2013) 1–10, https://doi.org/10.1109/TBCAS.2012.2192932.
[48] A. Müller, M.C. Wapler, U. Wallrabe, A quick and accurate method to determine the Poisson's ratio and the coefficient of thermal expansion of PDMS, Soft Matter 15 (2019) 779–784, https://doi.org/10.1039/c8sm02105h.
[49] K. Sun, P. Xie, Z. Wang, T. Su, Q. Shao, J.E. Ryu, X. Zhang, J. Guo, A. Shankar, J. Li, R. Fan, D. Cao, Z. Guo, Flexible polydimethylsiloxane/multi-walled carbon nanotubes membranous metacomposites with negative permittivity, Polymer (Guildf). 125 (2017) 50–57, https://doi.org/10.1016/j.polymer.2017.07.083.